ACS APPLIED MATERIALS & INTERFACES

Research Article

Cite This: ACS Appl. Mater. Interfaces 2018, 10, 35395−35403

www.acsami.org

Inch-Scale Grain Boundary Free Organic Crystals Developed by Nucleation Seed-Controlled Shearing Method

Zhiwen Zhou,[†] Zhichao Zhang,[†] Qisheng Wu,[‡,§] Xudong Ji,[†] Jinlan Wang,[‡,∥] Xiaocheng Zeng,[§] Shien-Ping Feng,[*,†] and Paddy Kwok Leung Chan[*,†]

[†]Department of Mechanical Engineering, The University of Hong Kong, Pok Fu Lam Road, Pokfulam, Hong Kong

[‡]School of Physics, Southeast University, Nanjing, Jiangsu 211189, P. R. China

[§]Department of Chemistry, University of Nebraska-Lincoln, Lincoln, Nebraska 68588, United States

[∥]Synergetic Innovation Center for Quantum Effects and Applications (SCIQEA), Hunan Normal University, Changsha, Hunan 410081, P. R. China

Supporting Information

ABSTRACT: Crystals of organic semiconductors are excellent candidates for flexible and array-based electronics. Large-scale synthesis of organic crystals in a controllable way while maintaining homogeneous single-crystal property has been a great challenge. The existence of grain boundaries and small crystal domains, however, restrict the device performance and limit the access to commercially viable organic electronics in the industry. Herein, we report the inch-scale synthesis of highly oriented 2,7-dioctyl[1]benzothieno[3,2-*b*][1]benzothiophene (C_8-BTBT) organic single crystal by nucleation seed-controlled shearing method. The organic field-effect transistors developed from such single crystal have excellent carrier mobility as high as 14.9 $cm^2\ V^{-1}\ s^{-1}$ and uniformity (standard deviation is 1.3 $cm^2\ V^{-1}\ s^{-1}$) of 225 devices. We also found that the rotation of the principal axis in the crystal is governed by the orientations of seeds and the possible mechanism behind this phenomenon is proposed based on the density functional theory calculations. We anticipate that this proposed approach will have great potential to be developed as a platform for the growth of organic crystals with high crystallinity on a large scale.

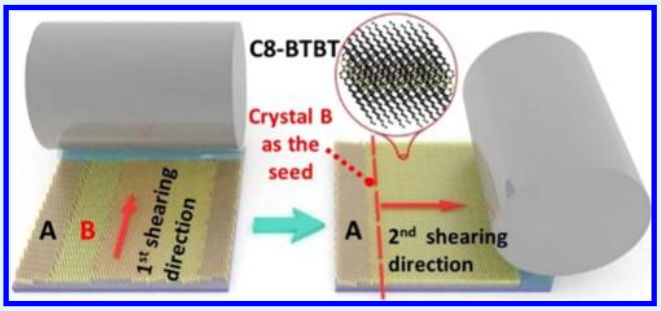

KEYWORDS: *grain boundary-free, single crystal, solution shearing, nucleation, organic field-effect transistor*

INTRODUCTION

Organic crystals are promising candidates for flexible and large-area electronics with the compatibility of solution deposition and low processing temperature under ambient air condition, which leads to low-cost mass manufacturing with a high throughput.[1,2] However, the involved nucleation and crystallization processes resulting from solvent evaporation and solute deposition will unavoidably introduce polycrystalline domains and grain boundaries in organic thin films.[3,4] As a result, the measured electrical performance of the solution-processed organic field-effect transistors (OFETs) are generally not the actual intrinsic properties of the organic molecules but obstructed by the grain boundaries and misalignment of the crystals. Depending on the levels of misalignment between the adjacent crystals, the transportation of carriers in these active layers would be deviated to different levels.[5,6] Other than the carrier mobility, the uniformity and reproducibility of the array devices would also suffer from uncontrolled grain boundaries. To our knowledge, these shortcomings are still the major obstacles to the utilization of the solution deposition for large-scale mass productions of OFETs. To develop organic crystals with higher quality, different approaches in solution processing such as guiding the recession of meniscus front,[7,8] controlling the nucleation site,[9,10] fabricating with the assistance of external forces,[11,12] or conducting preprocessing[13] and postprocessing[14] treatments have been applied in the OFET fabrications. Recently, a unique method of manufacturing wafer-scale and highly crystalline organic semiconductor (OSC) layers by introducing geometrical frustration has also been reported.[15,16] These methods can improve the quality of the organic thin film and device performance; however, a large-area, well-ordered, and grain boundary-free organic single crystal is yet to be demonstrated. As a result, to investigate the intrinsic properties of organic molecules and facilitate commercial manufactures,[17,18] there is a demand for the fabrication of well-ordered organic crystals on a largw scale without limitation from the effect of grain boundary defects. The large area of organic semiconductor single crystals not only improves the carrier mobility in OFETs but also allows them to be applied in the circuit,[19] and the long exciton

Received: June 11, 2018
Accepted: September 20, 2018
Published: September 20, 2018

DOI: 10.1021/acsami.8b09655
ACS Appl. Mater. Interfaces 2018, 10, 35395−35403

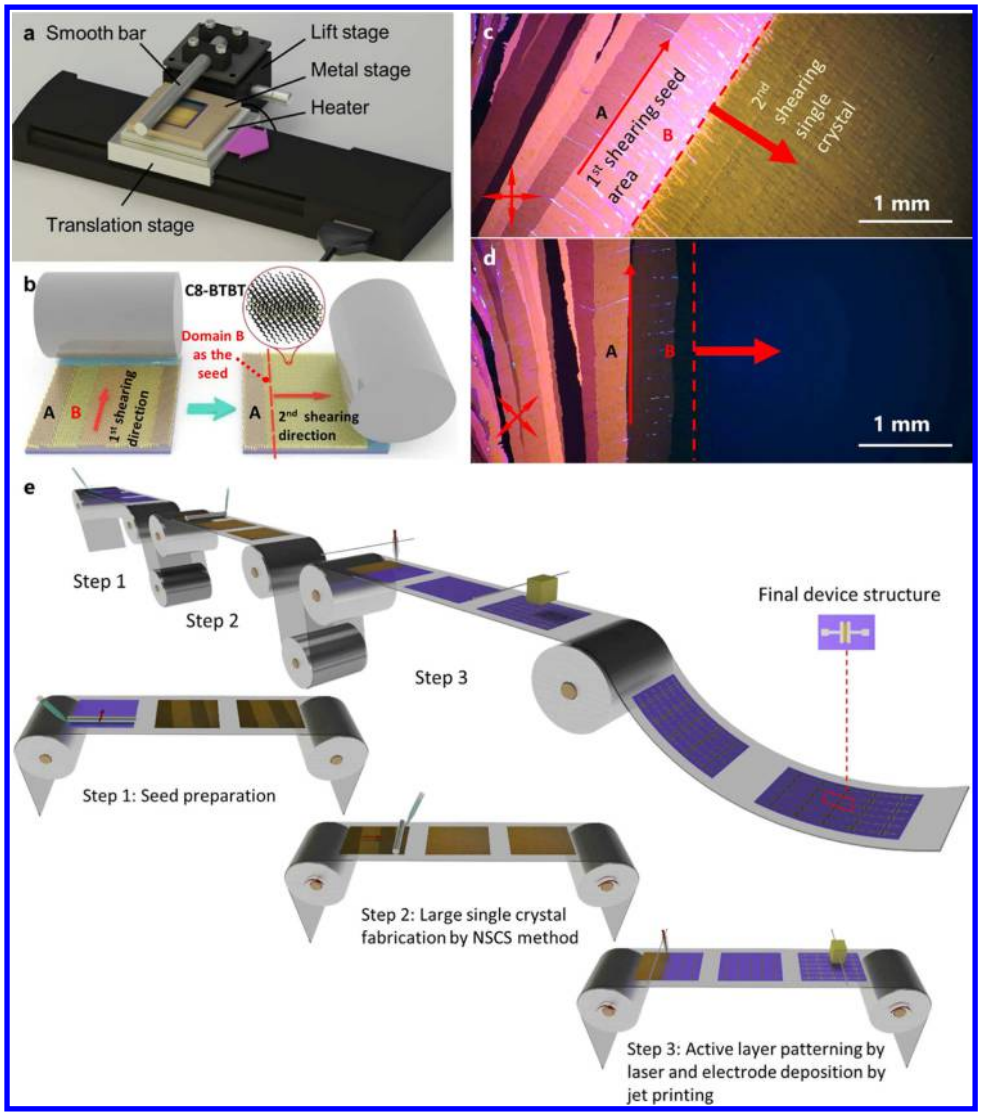

Figure 1. Nucleation seed-controlled shearing (NSCS) method. (a) Experimental setup for coating OSCs. (b) Schematic diagram for NSCS method, red arrows indicate shearing directions and dash line is where the second shearing begins. Crystal domain A and B have different molecular orientation deposited by first shearing process and crystal domain B is chosen as the seed for the second shearing process. (c, d) POM images of organic crystal sample coated by NSCS, the red arrows indicate shearing directions, and dash lines indicate the start of second shearing. (e) Schematic diagram of roll-to-roll application of our NSCS method.

diffusion length and high photoconductivity would also benefit other devices like optical sensors and organic photovoltaics.[20,21]

In our current studies, we reported a solution deposition method, known as nucleation seed-controlled shearing (NSCS), to fabricate grain boundary-free single crystal of a common organic semiconductor molecule, 2,7-dioctyl[1]benzothieno[3,2-*b*][1]benzothiophene (C_8-BTBT) up to inch scale. C_8-BTBT, a derivative of the BTBT family, has been utilized as the OFET active layer because of the good solubility in most organic solvents, compatibility with different solution-processing approaches, and high hole mobility.[22,23] Recently, by using the template-mediated molecular crystal seed, C_8-BTBT crystals up to millimeter scale with a mobility 10.4 $cm^2 V^{-1} s^{-1}$ have been demonstrated by spin coating.[10] Using the spin-coating method, C_8-BTBT has also been blended with p-dopants and polymer to develop OFETs with carrier mobility up to 13 $cm^2 V^{-1} s^{-1}$.[24] Crystalline C_8-BTBT obtained by combining the solution-processed templating layer with the lateral homoepitaxial growth by thermal evaporation shows a carrier mobility of up to 13.0 $cm^2 V^{-1} s^{-1}$.[25] Here, our NSCS method utilized the orienting crystals developed by first bar-coating as the seed and produce an inch-size single crystal by performing the second coating process nucleated from the seeds. To the best of our knowledge, this is the first report of the application of a nucleation seed in the shearing process to grow boundary-free and inch-size organic single crystals. NSCS is extremely sensitive to the orientations of the seeds where the second coating starts, and the direction of the second coating is perpendicular to the first coating. By eliminating the grain boundaries in the C_8-BTBT crystals, the device mobility shows a 40% increase. The excellent carrier mobility and uniformity are attributed to the inch-scale single crystal with high-density devices. Among 225 transistors tested, most of them showed similar transfer curves and the average mobility of 10.6 $cm^2 V^{-1} s^{-1}$. By regulating the orientations of the seeds, we realize that the principal axis of the C_8-BTBT crystal can be selectively rotated or remain unchanged along the crystals after second

DOI: 10.1021/acsami.8b09655
ACS Appl. Mater. Interfaces 2018, 10, 35395−35403

shearing, and the growth mechanism of the NSCS method is further explored by evaluating the surface energies from the density functional theory (DFT).

RESULTS AND DISCUSSION

The deposition of organic semiconductors (OSCs) crystallized thin film is carried out by a bar coating setup shown in Figure 1a. The trichloro(phenethyl)silane (PTS) treated Si/SiO_2 substrate is maintained at a constant temperature of 60 °C. Fifteen microliters of the OSC solution (8 mg/mL in *m*-xylene) is applied in the spacing between the bar and the substrate where the solution is pinned by capillary force. The influences on the C_8-BTBT crystals induced by various bar-coating parameters have been reported in our recent work.[12] Similarly, centimeters long and millimeter wide closely packed polycrystals are formed along the shearing direction after the first shearing. The boundaries of grains across different crystal domains after the first coating can be clearly observed under the polarized optical microscope (POM), as shown in Figure 1c. In the NSCS method, we utilize the second shearing to eliminate the boundaries inside the organic crystal film and unify the orientations of those crystal domains by turning them into a single crystal. The proposed method is inspired by the traditional Czochralski process and based on the seeded crystal enlarging growth,[26] which now is first realized in OSCs by solution shearing method. Figure 1b shows the schematic diagram of the two bar-coatings employed in the NSCS method. After the formation of the polycrystalline C_8-BTBT in the first coating (left side in Figure 1c), the substrate is rotated by 90° and one of the long crystal domains with a sharp boundary is then chosen to serve as the nucleation seed to start the second shearing process. The C_8-BTBT thin film formed after the second shearing turns into a single-crystal domain, as illustrated in Figure 1d. The crystal domain after second shearing (right side of Figure 1d) shows a uniform color without grain boundaries and has the same maximum and minimum brightness along the whole crystal domain (Video S1, Supporting Information). Limited by the size of the substrate we used, the largest single-crystal C_8-BTBT thin film we achieved on Si/SiO_2 substrate was around 2 in. × 2 in. (Figure S1, Supporting Information). Compared with the reported C_8-BTBT single crystals,[10,12] these single-crystal thin films are one of the largest sizes developed by solution processing. Our NSCS method has a high compatibility with industrial roll-to-roll processes, as shown in Figure 1e, accompanied by advantages of good uniformity and high reproducibility over a large area and low cost. We believe that this method will pave a new way for solution processing to deposit organic crystals and facilitate the commercialization of organic semiconductors with high solubility and high carrier mobility.

Figure 2a–c shows the POM and atomic force microscopy (AFM) results of the sample deposited by single bar shearing at a speed of 200 μm s^{-1}. From the POM images, it can be noticed that crystal domains with widths around 1 mm are formed along the shearing direction and have different orientations (Video S2, Supporting Information). The AFM results in Figure 2c,h show a very smooth surface with a root mean roughness of 0.2 nm in both single shearing and NSCS samples. Figure 2d,e shows the grazing incidence X-ray diffraction (GIXRD) in-plane scanning results and the (020) plane ϕ-scan by rotating the sample fabricated by single bar shearing. In all case, the associated angle of the (020) peak is

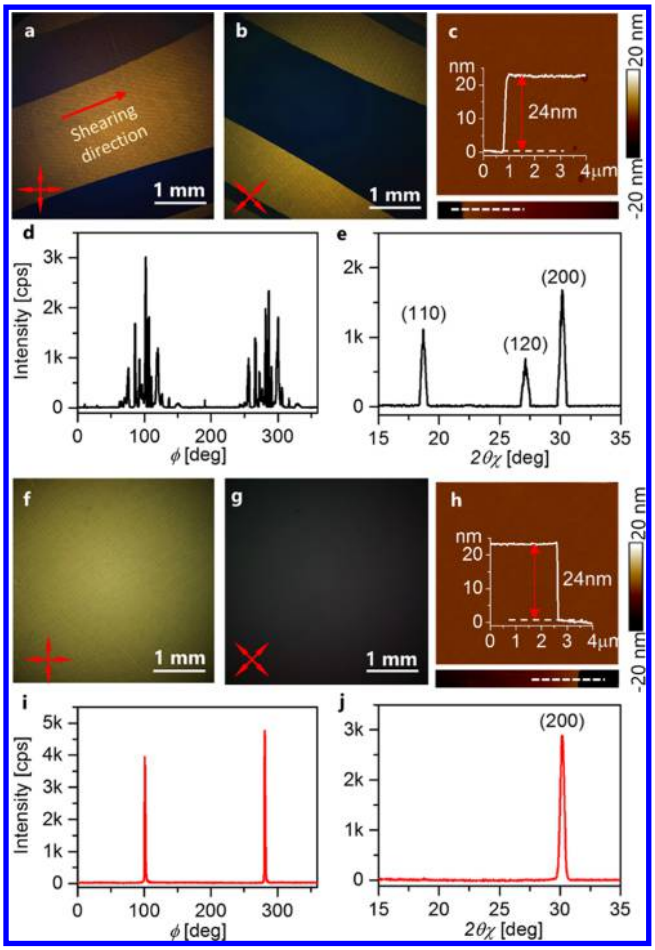

Figure 2. Characterizations of crystal films. The films are deposited by (a–e) single bar coating and (f–j) NSCS method. (a, b) and (f, g) POM images. (c, h) AFM images and film thickness measurement. (d, i) In-plane XRD results of the ϕ-scan of the (020) planes of the C_8-BTBT crystal. The grazing incident angle is 0.15°, and the associated angle of the (020) planes is 22.3°. (e, j) In-plane XRD results of $2\theta\chi$-scan of the (200) planes of the C_8-BTBT crystal. The grazing incident angle is 0.15° and 2θ is 0.3°.

kept at 22.3°, if without further notification. The schematics of the GIXRD in-plane phi-scan measurement of (020) planes are shown in Figure S2 (Supporting Information). As the X-ray incident angle is aligned with the first shearing direction of the sample, the (020) peaks in the ϕ-scan are in the vicinity of 101 and 281° (Figure 2d), indicating that the (020) planes are roughly perpendicular to the shearing direction, i.e., *b*-axis is more preferred along with the shearing direction. The multiple peaks in the ϕ-scan of the (020) planes (Figure 2d) and the presence of the (110) and (120) peaks in the (200) plane detection setting (Figure 2e) also suggest that the crystal domains are not perfectly aligned and have different molecular orientations. In contrast, the uniform color of the POM images of the NSCS samples in Figure 2f,g suggests that a single crystal covers whole of the substrate except the edge. The two sharp Bragg peaks in the ϕ-scan of the (020) planes detection (Figure 2i) and the single sharp peak in the in-plane XRD spectrum of the (200) peak detection (Figure 2j) confirm the perfect single crystal property of the C_8-BTBT thin film. The position of the (020) peaks in the ϕ-scan indicates the crystal follows the orientation of nucleation seed completely and the *a*-axis is along the second shearing direction. The crystal

DOI: 10.1021/acsami.8b09655
ACS Appl. Mater. Interfaces 2018, 10, 35395–35403

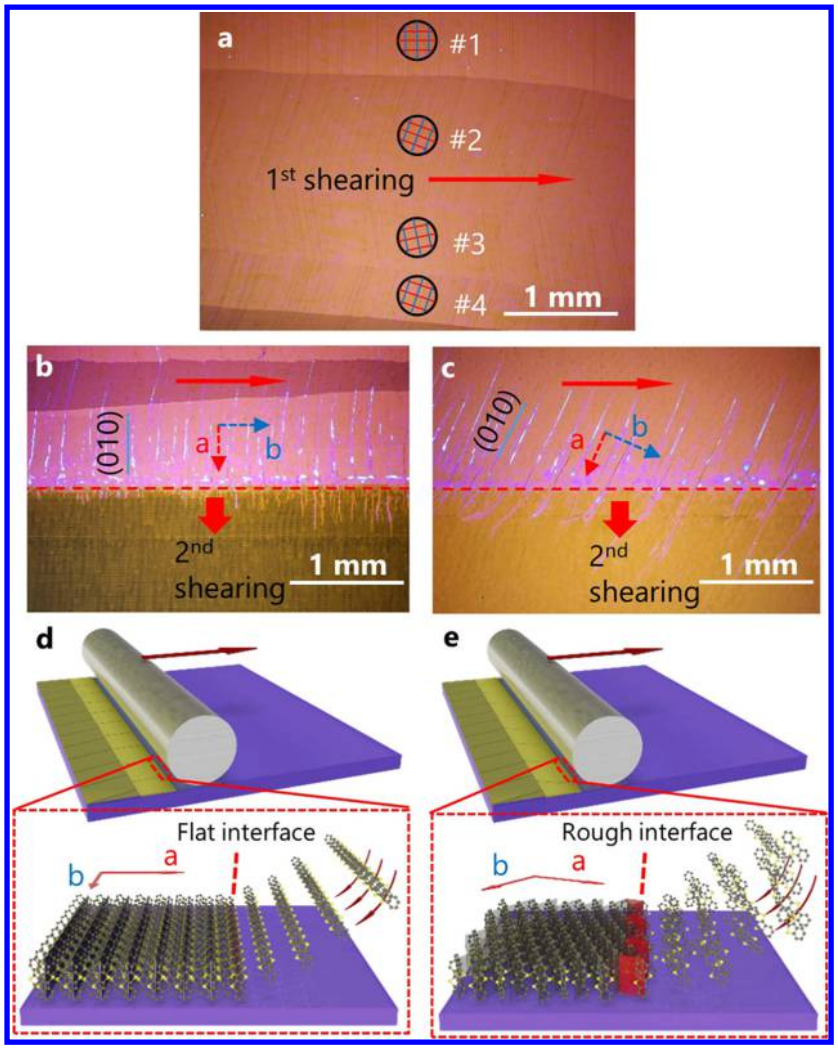

Figure 3. Two cases of single crystals from second shearing. (a) Crystals and their orientations by first time shearing. The orientations are determined by cracks on the crystals and colors under POM. Circular symbols are used to represent the orientation of the crystals, where red parallel lines represent the (100) plane and blue parallel lines represent the (010) plane. (b) The POM image of the start part of a large crystal nucleated from similar crystal domain #1 in (a), with crystal growth following the molecular orientation in seed crystal. (c) The POM images of the start part of a large crystal nucleated from similar crystal domain #2 in (a), with a gradual shift of orientation observed. (d) The schematic diagram of sequential crystal growth follows the flat nucleation seed crystal in the NSCS method. (e) The schematic diagram of asymmetric crystal growth caused by an irregular interface between the seed crystal and the solution.

growth mechanism in the second shearing process resembles that of inorganic single-crystal semiconductors such as silicon and germanium fabricated by the Czochralski method.[27] We also studied and found that the deposition temperature, solution concentration, and shearing speed of the second shearing have similar effects on the thickness and morphology of the C_8-BTBT crystals. Here, we only included the effects of different shearing speeds of both first and second shearing, which are shown in Figures S3 and S4 (Supporting Information). It can be observed from Figure S4 that the coating speed in the second shearing process directly determines the thickness and morphology of the C_8-BTBT thin film. A higher speed is not favorable to getting a compact film; also, lower speed will result in a thicker layer with cracks on the surface. These cracks are parallel to *a*-axis, i.e., the (010) planes of the C_8-BTBT crystals.[28] The determination of the cracks could be the anisotropic thermal contraction of the C_8-BTBT crystal.[28] A smaller Young's modulus (E, E_a = 20.51 GPa; E_b = 15.53 GPa) along the *b*-axis of the C_8-BTBT will induce a larger thermal contraction strain in the *b*-direction, resulting in cracking along the (010) planes.[29] From our DFT calculations (see Experimental Methods for details) of the low-index planes of the C_8-BTBT crystal shown in Figure S5 (Supporting Information), it can be noticeed that the (010) planes have the lowest surface energy of 2.76 meV $Å^{-2}$; thus, they are expected to have craks along the (010) planes in the C_8-BTBT due to weakest adhesion.[30,31] It also further verifies that the shearing direction is along the *b*-axis because the cracks in most single-crystal domains are perpendicular to the shearing direction in the single shearing process. The effect on the second coating speed is shown in Figure S4 (Supporting Information). Deposition of large single crystals are succeeded in all the coating speeds from 100 to 300 $\mu m\ s^{-1}$, successfully demonstrating the controllable thickness from tens of layers to few layers. It is important to notice that the thickness of the single-crystal thin film developed at a specific speed after the second coating speed is very similar to the polycrystalline film deposited by single coating at the same speed. We believed in the NSCS method in which the second coating direction has a 90° difference from the first one, the larger volume of the

DOI: 10.1021/acsami.8b09655
ACS Appl. Mater. Interfaces 2018, 10, 35395−35403

solvent right underneath the coating bar will dissolve and redeposit the C_8-BTBT molecules, as illustrated in Figure S6 (Supporting Information). The seed crystal near the meniscus will facilitate the nucleation of the dissolved C_8-BTBT molecules by regulating the alignment of the redeposit molecules to form a larger single-crystal domain. The proposed crystal formation mechanism based on the intermolecular interaction aspects will be discussed in the following section.

In this part, we will investigate the formation mechanism of the large-area single crystal by verifying the importance of the seeding crystal orientation in the NSCS method and the corresponding surface energies of different crystal planes by DFT. The POM image in Figure 3a shows four crystal domains with different alignments to the first shearing direction. Domain 1 has the *b*-axis parallel to the shearing direction, whereas domains 2 and 4 has 19° of clockwise shift and domain 3 has 12° of anticlockwise shift. In the NSCS approach, as mentioned before, we intentionally located the seed regions at crystals like domain 1 as the starting point of the second coating seen in Figure 3b. Here, we will discuss the observations if we start the second coating at the tilted crystal domains like #2, #3, and #4 with tilted cracks along the second shearing direction as shown in Figure 3c. The first observation is that large-size single domains can still be formed without noticeable grain boundaries. However, instead of having the same crystal orientation in the whole crystal domain as the seeding crystal, we found the deposited C_8-BTBT developed from the tilted seed crystal will have a gradual orientation change along the second shearing direction. It seems that the crystal consists of myriad low-angle grain boundaries and the *b*-axis of the crystal will gradually move toward the shearing direction during the crystal growth, i.e., the second coating behaves like the first shearing and the deposited crystal has *b*-axis aligned with the shearing direction in the end. This trend can also be observed by the gradual brightness change in Video S3 (Supporting Information). A gradual change in brightness can be observed if the second coating starts at domain #2, and a total 33° shift was measured under the polarized microscope in a 2 cm long crystal sample. This agrees well with the in-plane XRD ϕ-scan results, as shown in Figure S7 (Supporting Information), where two broad peaks with a width around 35° can be observed.

In the traditional Czochralski method, the quality of the prepared crystals is affected by the shape of the liquid−solid interface during the growth process.[32] It is well known that good quality crystals are obtained when the interface is flat, where the irregular interface could lead to undesirable defects, such as gas bubble entrapment, strains, cracks, inhomogeneous of impurities, and low-angle grain boundaries.[33] Based on these, we proposed a possible crystal formation mechanism based on the intermolecular interaction in the solid−liquid interface. The plausible mechanism behind such an effect of seed orientation on crystal growth is indicated in Figure 3d,e. In the NSCS method, the regular cracks in the seed crystal are parallel to the second shearing direction. This implies that the solvent redissolved the deposited crystal and the exposed cross-sectional facet is (100) plane, which provides a basis for nucleation sites for free C_8-BTBT molecules in the solute to grow and follow the molecular orientation in the seed crystal. However, with a tilted seed crystal in which regular (010) plane cracks are not aligned with the second shearing direction, irregular facet interface between the seed crystal and the solution will be formed, which will cause asymmetric growth rate of the crystals during the redeposition process and thus the seeding effect will disappear gradually. As a result, the orientation of the crystal will slowly shift back to the configuration just like the first bar coating and the *b*-axis tends to align with the shearing direction. Generally, the facets with low surface energy tend to be visible during the solution-dissolving process, and it is reported that high-index facets are usually more reactive, possessing higher surface energy, compared with low-index crystal planes of the same crystal.[34] From the DFT calculations of the low-index planes of the C_8-BTBT crystal as shown in Figure S5 (Supporting Information), it is noticeable that the (010), (110), and (100) planes have a relatively low surface energy; thus, we confidently speculate these low-index crystal planes will be exposed as the interface between the seed crystal and the solution during the second shearing process. To further confirm this phenomenon, we intentionally dripped 5 μL pure *m*-xylene solvent on the top of the C_8-BTBT crystal film and observed the dissolving process under a polarizing microscope at room temperature. As shown in Video S4 (Supporting Information), the exposed cracks along the (010) and (100) planes of the C_8-BTBT are clearly observed due to the low surface energy of these crystals planes. The surface energy of (100) planes is a local minimum energy site with the energy 4.21 meV $Å^{-2}$, which is a bit larger than that of (010) planes. Although the exposed (110) planes of the C_8-BTBT are not observed directly, we believe they will be formed during the second shearing process, which might require more advanced microscopic analysis. In short, we believe the orientation of the seeding crystal plays a critical role in providing an easier nucleation path and a well-ordered crystal growth by reducing the nucleation energy barrier in the NSCS method. It is the first time that we observe and confirm these phenomena in organic single-crystal fabrication process based on the pure organic solvent.

The statistical studies of 40 C_8-BTBT single-crystal bottom-gate top-contact OFETs fabricated by NSCS and single bar coating on two 1.5 cm × 1.5 cm substrates are shown in Figure 4. In these devices, silver and 2,3,5,6-tetrafluoro-7,7,8,8-tetracyanoquinodimethane (F4-TCNQ) are deposited as the top electrode and the charge injection layer onto OSCs by thermal evaporation in a vacuum. The channel length and width are 250 and 500 μm, respectively. The field-effect characteristics of the devices were measured in a nitrogen glovebox at room temperature. As mentioned before, we confirmed that the *b*-axis of the deposited C_8-BTBT crystals is along the shearing direction of the single bar coating. Similarly, in the second shearing of the NSCS method, as the shearing direction is perpendicular to the first shearing, it is along the *a*-axis of the crystal. Here, the field effect mobility along the *a*-axis of the C_8-BTBT crystal is primarily discussed below because the grain boundaries are generally aligned to the first shearing direction. It can be noticed that the single-crystal OFETs deposited by NSCS show high and very uniform performance. The averaged *a*-axis mobility of the crystals is improved from 8.9 $cm^2 V^{-1} s^{-1}$ (highest 11.5 $cm^2 V^{-1} s^{-1}$) to 12.5 $cm^2 V^{-1} s^{-1}$ (highest 14.9 $cm^2 V^{-1} s^{-1}$) while switching from single coating to the NSCS method (Figure 4a,d). This value is on the high side for the best few reported C_8-BTBT OFETs fabricated by other solution methods.[10,23,35−37] For the same C_8-BTBT semiconductor, the reported C_8-BTBT still shows a strong variation among different methods. One of the major reason is the nonideal transfer curves where "kinks" or change in slope is present, which would lead to a certain

DOI: 10.1021/acsami.8b09655
ACS Appl. Mater. Interfaces 2018, 10, 35395−35403

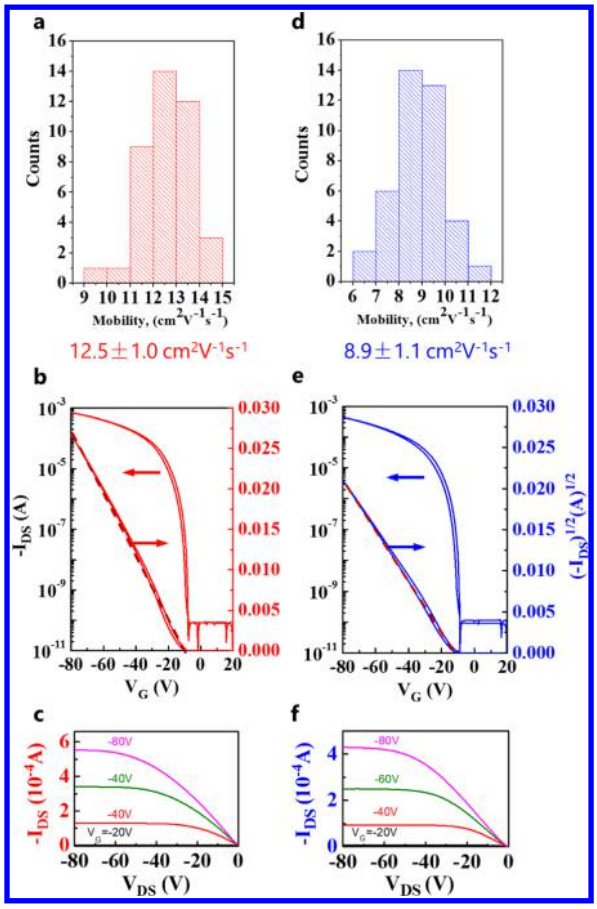

Figure 4. Comparison of performance of OFETs based on inch-size single-crystal films deposited by NSCS method (red) and millimeter-scale crystal films deposited by single bar coating (blue). (a, d) Statistic histograms of the charge carrier mobility measured along the *a*-axis of the C8-BTBT crystal obtained from 40 devices. (b, e) Typical transfer curves plot on the same scale. (c, f) The corresponding output curves.

amount of error in estimating the carrier mobility. In our current report, the square-root plot of I_{DS} against V_G is linear without the slope change. We utilized a channel of 250 μm, which can suppress the contact resistance effect. We attributed the high performance to the boundary-free channels and high crystallinity of C_8-BTBT as the active layers. It is worth pointing out that the grain boundary effect on the carrier mobility of C_8-BTTB is not as strong as that of other materials like *N*,*N*′-bis(*n*-octyl)-(1,7 & 1,6)-dicyanoperylene-3,4:9,10-bisdicarboximide (PDI8-CN_2) in which mobility drop of nearly 2 orders of magnitude has been observed.[5] The devices also has a high on/off ratio of about 10^7 and a relatively smaller threshold voltage (V_{th}), nearly −15 V, compared with other reported C_8-BTBT-based transistors using SiO_2 as the dielectric layer.[37,38] The small hysteresis indicates low shallow trap densities at the interface between the semiconductor and the dielectric. Recently, more and more attention has been paid to the overestimation of the extracted charge carrier mobility in OFETs due to gated contacts[39] and some critical guidelines such as calculating the reliability factor *r* are proposed by Podzorov and co-workers.[40] Based on these, we measured the reliability factor of the device in our work and the value of *r* is around the 70%. In addition, the high uniformity of electrical performances is proofed by the statistic study of transistor characteristics over 40 devices, as shown in Figure S8 (Supporting Information). We have also studied the mobility anisotropy along the *a*-axis and *b*-axis of the C_8-BTBT films deposited by NSCS and single bar coating methods. From Table S1 (Supporting Information), we can observe that the field-effect mobility along the *a*-axis is higher than that along the *b*-axis in both cases, which is consistent with the observations in our previous study.[12] This anisotropy can also be supported by previous work done by Takeya and co-workers, who utilized the transfer integral to show the carrier mobility in the *a*-axis of the C_8-BTBT crystal is higher than that in the *b*-axis.[41] Meanwhile, the mobilities along the *b*-axis are comparable in both cases, which is quite reasonable because the morphology and thickness are almost the same in these two cases under the same shearing speed. It is important to notice that in the OFETs based on the polycrystalline C_8-BTBT films deposited by single bar coating method, the channels in the *a*-axis direction would come across the grain boundaries; however, we still see the similar trend that the *a*-axis has a higher mobility. In addition, the NSCS-deposited single crystal has better uniformity and its trap density decreases by over 25% due to the absence of grain boundaries.

The excellent potential of our NSCS method in the large-scale production of OFETs or integrated circuit is further demonstrated by scaling up to an inch-scale single crystal with a high device density. The optical image of the sample is shown in Figure 5a, and the corresponding polarized optical micrograph images are exhibited in Figure 5b,c. The high quality of the produced inch-size single-crystal film was checked by the simultaneous color change of the entire film from bright to dark with rotation of the substrate, indicating the absence of any grain boundaries in the film. As shown in Figure 5d,e, most of the 225 OFETs tested exhibited similar transfer curves and the plotted carrier mobility distribution with quite a uniform color coverage represents the uniformity of electrical performance of these devices with an average mobility of 10.6 $cm^2\ V^{-1}\ s^{-1}$. The uniform mobility color map clearly demonstrates the high compatibility of the fancifully proposed NSCS method for the industrial roll-to-roll application of large-area electronics.

CONCLUSIONS

In summary, we have developed a new strategy to develop inch-scale and grain boundary-free C_8-BTBT crystals via controlling the nucleation seed and thus the crystal growth. The critical feature of our NSCS method is the predeposited crystal domains developed by first shearing, which play an important role in guiding the further nucleation of the sequential molecules in the second shearing. It can reduce the nucleation energy barrier, as well as suppress the random and spontaneous nucleation and crystal growth processes. The OFETs based on the inch-scale single crystal show good uniformity and high yield with a low trap state density, and the highest mobility is up to 14.9 $cm^2\ V^{-1}\ s^{-1}$. We believe the mechanism of an introduction of crystal seeds with specific orientation is a valuable key for the development of a well-ordered organic crystal and large-scale manufacturing of organic semiconductors. The NSCS approach is a cornerstone for practical application of OFETs in large-area sensors or backplanes of displays through roll-to-roll or direct printing mass production.

DOI: 10.1021/acsami.8b09655
ACS Appl. Mater. Interfaces 2018, 10, 35395−35403

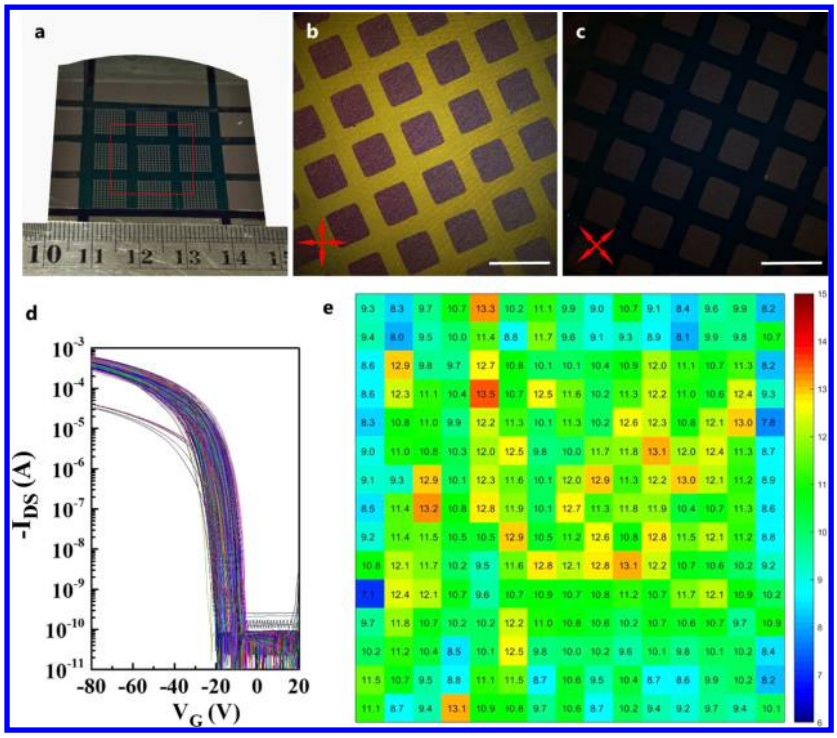

Figure 5. Statistic study of the uniformity of electrical performance based on an inch-size single-crystal film. (a) Optical image of an inch-size single crystal with high density devices. (b, c) Polarized optical micrograph of the inch-size single crystal with dense devices, and the scale bar is 1 mm. (d) Transfer curves of 225 devices located in the marked region in the (a) with good uniformity, average mobility is around 10.6 $cm^2 V^{-1} s^{-1}$. (e) Mobility distribution of the all 225 devices, there are only two passable devices with mobility slightly lower than 8 $cm^2 V^{-1} s^{-1}$.

EXPERIMENTAL METHODS

Materials. Silicon substrates with 300 nm silicon dioxide were bought from University Wafer Inc. High-purity C_8-BTBT (99.5 %) was obtained from Luminescence Technology Corp. Solvents and other materials were purchased from Sigma-Aldrich.

Nucleation Seed-Controlled Shearing Deposition. We assembled the bar coating setup ourselves, and the details of the setup are accessible in our previous work.[35] The substrate was kept at 60 °C for both first and second shearings. When the first shearing finished, the substrate was rotated by 90° and the second shearing started from the chosen seed crystal. After deposition, the samples are transferred to a vacuum oven for more than 5 h to eliminate residue solvents. The optimized shearing condition is 100 $\mu m\ s^{-1}$ for the first shearing and 200 $\mu m\ s^{-1}$ for the second shearing.

Characterizations. The POM images are obtained from polarized optical microscope model Nikon Eclipse LV100N. The orientations of different crystal domains can be indicated by POM due to the fact that small regular cracks will be seen under the microscope when the coated crystal layer gets thicker by slow shearing speed. For C_8-BTBT, cracks are formed along the *a*-axis, which has already been confirmed by our in-plane XRD results and investigations from other groups. Atomic force microscopy (AFM) images were captured by Multi-Mode 8 from Bruker. The XRD results are measured by Rigaku SmartLab X-Ray diffractometer with the highest power of 9 kW. Grazing incident angle of $\omega = 0.15°$ was used for the in-plane test. The samples were cut into 1.5 cm × 1.5 cm size before testing.

OFETs Fabrication and Measurement. Silicon substrate was cleaned by standard substrate cleaning procedure including oxygen plasma treatment, which has been reported before.[35] The silicon dioxide surface was treated by the PTS solution at 90 °C for 2 h. The deposition speed we used ranged between 100 and 300 $\mu m\ s^{-1}$. For the source/drain electrodes, we utilized 50 nm silver with 3 nm F4-TCNQ charge injection layer deposited by thermal evaporation. The W/L ratio is 2 (W is 500 μm and L is 250 μm). All the testing were performed under a nitrogen environment and the detailed testing procedures can be found in our previous work.[35] The trap state density is evaluated by $N_{it} = C_i(SSq/k_BT \ln 10^{-1})/q$,[42] where T is the absolute temperature, SS is the subthreshold swing, q is the elementary charge, and k_B is Boltzmann constant.

Details of DFT Calculations. All the DFT calculations were carried out by using density functional theory method with projector-augmented-wave[43] pseudopotentials as implemented in Vienna ab initio simulation 5.4 package.[44] Perdew–Burke–Ernzerhof parametrization of the generalized gradient approximation[45] was employed. The effect of vdW interactions was described with the semiempirical correction scheme of Grimme, DFT-D2.[46] The cutoff energy of plane-wave 520 eV and a vacuum space larger than 12 Å were used in the simulations. The product of lattice constants and k points was set to be larger than 40 for sampling the first Brillouin zone. The systems are completely relaxed until the energy and force were converged to 10^{-5} eV and 0.02 eV/Å.

ASSOCIATED CONTENT

Supporting Information

The Supporting Information is available free of charge on the ACS Publications website at DOI: 10.1021/acsami.8b09655.

Optical image of the inch-size single-crystal sample, schematic of GIWXRD, POM images and AFM images of the samples deposited by different first and second shearing speeds, DFT results, schematic of dissolution during the second shearing, POM images and corresponding XRD results of the crystals with rotated molecular orientation, transfer curves of OFETs, and the table of performance of OFETs by single bar shearing and NSCS method (PDF)

Inch-size single crystal fabricated by NSCS method (Movie S1) (AVI)

Polycrystal fabricated by general single bar shearing method (Movie S2) (AVI)

DOI: 10.1021/acsami.8b09655
ACS Appl. Mater. Interfaces 2018, 10, 35395–35403

Large-scale crystal with rotated molecular orientation (Movie S3) (AVI)

Dissolving C_8-BTBT crystal by pure *m*-xylene solvent (Movie S4) (AVI)

AUTHOR INFORMATION

Corresponding Authors

*E-mail: hpfeng@hku.hk (S.-P.F.).
*E-mail: pklc@hku.hk (P.K.L.C.).

ORCID

Jinlan Wang: 0000-0002-4529-874X
Xiaocheng Zeng: 0000-0003-4672-8585
Shien-Ping Feng: 0000-0002-3941-1363
Paddy Kwok Leung Chan: 0000-0002-3166-2192

Notes

The authors declare no competing financial interest.

ACKNOWLEDGMENTS

Z.Z. and Z.Z. contributed equally to this work. P.K.L.C. thanks the support from the General Research Fund (GRF) under Grant No. HKU 17264016, the NSFC/RGC Joint Research Scheme under Grant No. HKU 715/14. J.W. is supported by the National Key Research and Development Program of China (No. 2017YFA0204800). Q.W. is supported by China Scholarship Council (CSC, 201606090079). X.Z. is supported by a grant from Nebraska Center for Energy Sciences Research and a fund from Beijing Advanced Innovation Center for Soft Matter Science & Engineering for summer visiting scholar. The computational resources utilized in this research were provided by National Supercomputing Center in Tianjin, NC3 computer facility and Holland Supercomputing Center in the University of Nebraska-Lincoln.

REFERENCES

(1) Gundlach, D. J.; Royer, J. E.; Park, S.; Subramanian, S.; Jurchescu, O.; Hamadani, B. H.; Moad, A.; Kline, R. J.; Teague, L.; Kirillov, O.; et al. Contact-Induced Crystallinity for High-Performance Soluble Acene-Based Transistors and Circuits. *Nat. Mater.* **2008**, *7*, 216−221.

(2) Zhang, X.; Jie, J.; Deng, W.; Shang, Q.; Wang, J.; Wang, H.; Chen, X.; Zhang, X. Alignment and Patterning of Ordered Small-Molecule Organic Semiconductor Micro-/Nanocrystals for Device Applications. *Adv. Mater.* **2016**, *28*, 2475−2503.

(3) Sakanoue, T.; Sirringhaus, H. Band-Like Temperature Dependence of Mobility in A Solution-Processed Organic Semiconductor. *Nat. Mater.* **2010**, *9*, 736−740.

(4) Diao, Y.; Shaw, L.; Bao, Z.; Mannsfeld, S. C. Morphology Control Strategies for Solution-Processed Organic Semiconductor Thin Films. *Energy Environ. Sci.* **2014**, *7*, 2145−2159.

(5) Rivnay, J.; Jimison, L. H.; Northrup, J. E.; Toney, M. F.; Noriega, R.; Lu, S.; Marks, T. J.; Facchetti, A.; Salleo, A. Large Modulation of Carrier Transport by Grain-Boundary Molecular Packing and Microstructure in Organic Thin Films. *Nat. Mater.* **2009**, *8*, 952−958.

(6) Lee, S. S.; Mativetsky, J. M.; Loth, M. A.; Anthony, J. E.; Loo, Y.-L. Quantifying Resistances across Nanoscale Low-and High-Angle Interspherulite Boundaries in Solution-Processed Organic Semiconductor Thin Films. *ACS Nano* **2012**, *6*, 9879−9886.

(7) Mitsui, C.; Okamoto, T.; Yamagishi, M.; Tsurumi, J.; Yoshimoto, K.; Nakahara, K.; Soeda, J.; Hirose, Y.; Sato, H.; Yamano, A.; et al. High-Performance Solution-Processable N-Shaped Organic Semiconducting Materials with Stabilized Crystal Phase. *Adv. Mater.* **2014**, *26*, 4546−4551.

(8) Li, H.; Tee, B. C.; Cha, J. J.; Cui, Y.; Chung, J. W.; Lee, S. Y.; Bao, Z. High-Mobility Field-Effect Transistors from Large-Area Solution-Grown Aligned C_{60} Single Crystals. *J. Am. Chem. Soc.* **2012**, *134*, 2760−2765.

(9) Goto, O.; Tomiya, S.; Murakami, Y.; Shinozaki, A.; Toda, A.; Kasahara, J.; Hobara, D. Organic Single-Crystal Arrays from Solution-Phase Growth Using Micropattern with Nucleation Control Region. *Adv. Mater.* **2012**, *24*, 1117−1122.

(10) Kwon, S.; Kim, J.; Kim, G.; Yu, K.; Jo, Y. R.; Kim, B. J.; Kim, J.; Kang, H.; Park, B.; Lee, K. Organic Single-Crystal Semiconductor Films on A Millimeter Domain Scale. *Adv. Mater.* **2015**, *27*, 6870−6877.

(11) Diemer, P. J.; Lyle, C. R.; Mei, Y.; Sutton, C.; Payne, M. M.; Anthony, J. E.; Coropceanu, V.; Brédas, J. L.; Jurchescu, O. D. Vibration-Assisted Crystallization Improves Organic/Dielectric Interface in Organic Thin-Film Transistors. *Adv. Mater.* **2013**, *25*, 6956−6962.

(12) Zhang, Z.; Peng, B.; Ji, X.; Pei, K.; Chan, P. K. L. Marangoni-Effect-Assisted Bar-Coating Method for High-Quality Organic Crystals with Compressive and Tensile Strains. *Adv. Funct. Mater.* **2017**, *27*, No. 1703443.

(13) Giri, G.; Park, S.; Vosgueritchian, M.; Shulaker, M. M.; Bao, Z. High-Mobility, Aligned Crystalline Domains of TIPS-Pentacene with Metastable Polymorphs Through Lateral Confinement of Crystal Growth. *Adv. Mater.* **2014**, *26*, 487−493.

(14) Liu, C.; Minari, T.; Lu, X.; Kumatani, A.; Takimiya, K.; Tsukagoshi, K. Solution-Processable Organic Single Crystals with Bandlike Transport in Field-Effect Transistors. *Adv. Mater.* **2011**, *23*, 523−526.

(15) Hamai, T.; Arai, S.; Minemawari, H.; Inoue, S.; Kumai, R.; Hasegawa, T. Tunneling and Origin of Large Access Resistance in Layered-Crystal Organic Transistors. *Phys. Rev. Appl.* **2017**, *8*, No. 054011.

(16) Arai, S.; Inoue, S.; Hamai, T.; Kumai, R.; Hasegawa, T. Semiconductive Single Molecular Bilayers Realized Using Geometrical Frustration. *Adv. Mater.* **2018**, *30*, No. 1707256.

(17) Hulea, I. N.; Fratini, S.; Xie, H.; Mulder, C.; Iossad, N.; Rastelli, G.; Ciuchi, S.; Morpurgo, A. Tunable Fröhlich Polarons in Organic Single-Crystal Transistors. *Nat. Mater.* **2006**, *5*, 982−986.

(18) Reyes-Martinez, M. A.; Crosby, A. J.; Briseno, A. L. Rubrene Crystal Field-Effect Mobility Modulation via Conducting Channel Wrinkling. *Nat. Commun.* **2015**, *6*, No. 6948.

(19) Yamamura, A.; Watanabe, S.; Uno, M.; Mitani, M.; Mitsui, C.; Tsurumi, J.; Isahaya, N.; Kanaoka, Y.; Okamoto, T.; Takeya, J. Wafer-Scale, Layer-Controlled Organic Single Crystals for High-Speed Circuit Operation. *Sci. Adv.* **2018**, *4*, No. eaao5758.

(20) Najafov, H.; Lee, B.; Zhou, Q.; Feldman, L.; Podzorov. Observation of Long-Range Exciton Diffusion in Highly Ordered Organic Semiconductors. *Nat. Mater.* **2010**, *9*, 938−943.

(21) Baeg, K. J.; Binda, M.; Natali, D.; Caironi, M.; Noh, Y. Y. Organic Light Detectors: Photodiodes and Phototransistors. *Adv. Mater.* **2013**, *25*, 4267−4295.

(22) Izawa, T.; Miyazaki, E.; Takimiya, K. Molecular Ordering of High-Performance Soluble Molecular Semiconductors and Re-evaluation of Their Field-Effect Transistor Characteristics. *Adv. Mater.* **2008**, *20*, 3388−3392.

(23) Minemawari, H.; Yamada, T.; Matsui, H.; Tsutsumi, J.; Haas, S.; Chiba, R.; Kumai, R.; Hasegawa, T. Inkjet Printing of Single-Crystal Films. *Nature* **2011**, *475*, 364−367.

(24) Paterson, A. F.; Treat, N. D.; Zhang, W.; Fei, Z.; Wyatt-Moon, G.; Faber, H.; Vourlias, G.; Patsalas, P. A.; Solomeshch, O.; Tessler, N.; et al. Small Molecule/Polymer Blend Organic Transistors with Hole Mobility Exceeding 13 $cm^2\ V^{-1}\ s^{-1}$. *Adv. Mater.* **2016**, *28*, 7791−7798.

(25) Janneck, R.; Pilet, N.; Bommanaboyena, S. P.; Watts, B.; Heremans, P.; Genoe, J.; Rolin, C. Highly Crystalline C8-BTBT Thin-Film Transistors by Lateral Homo-Epitaxial Growth on Printed Templates. *Adv. Mater.* **2017**, *29*, No. 1703864.

(26) Vlassiouk, I. V.; Stehle, Y.; Pudasaini, P. R.; Unocic, R. R.; Rack, P. D.; Baddorf, A. P.; Ivanov, I. N.; Lavrik, N. V.; List, F.; Gupta, N.;

DOI: 10.1021/acsami.8b09655
ACS Appl. Mater. Interfaces 2018, 10, 35395−35403

et al. Evolutionary Selection Growth of Two-Dimensional Materials on Polycrystalline Substrates. *Nat. Mater.* **2018**, *17*, 318−322.
(27) Schmehr, J. L.; Wilson, S. D. Active Crystal Growth Techniques for Quantum Materials. *Annu. Rev. Mater. Res.* **2017**, *47*, 153−174.
(28) Fesenko, P.; Rolin, C.; Janneck, R.; Bommanaboyena, S. P.; Gaethje, H.; Heremans, P.; Genoe, J. Determination of Crystal Orientation in Organic Thin Films Using Optical Microscopy. *Org. Electron.* **2016**, *37*, 100−107.
(29) Xi, J.; Long, M.; Tang, L.; Wang, D.; Shuai, Z. First-Principles Prediction of Charge Mobility in Carbon and Organic Nanomaterials. *Nanoscale* **2012**, *4*, 4348−4369.
(30) Wiederhorn, S. M. Fracture Surface Energy of Glass. *J. Am. Ceram. Soc.* **1969**, *52*, 99−105.
(31) Sernicola, G.; Giovannini, T.; Patel, P.; Kermode, J. R.; Balint, D. S.; Britton, T. B.; Giuliani, F. In Situ Stable Crack Growth at the Micron Scale. *Nat. Commun.* **2017**, *8*, No. 108.
(32) Kusuma, H.; Made, D.; Sudin, M.; Rohani, M. In *The Growth and Growth Mechanism of Congruent LiNbO3 Single Crystals by Czochralski Method*, AIP Conf. Proc.; AIP, 2010; pp 182−186.
(33) Santos, M.; Rojo, J.; Cintas, A.; Arizmendi, L.; Diéguez, E. Changes in the Solid-Liquid Interface during the Growth of Bi12SiO20, Bi12GeO20 and LiNbO3 Crystals Grown by the Czochralski Method. *J. Cryst. Growth* **1995**, *156*, 413−420.
(34) Chang, J.; Ahmed, R.; Wang, H.; Liu, H.; Li, R.; Wang, P.; Waclawik, E. R. ZnO Nanocones with High-Index $\{10\bar{1}1\}$ Facets for Enhanced Energy Conversion Efficiency of Dye-Sensitized Solar Cells. *J. Phys. Chem. C* **2013**, *117*, 13836−13844.
(35) Zhang, F.; Dai, X.; Zhu, W.; Chung, H.; Diao, Y. Large Modulation of Charge Carrier Mobility in Doped Nanoporous Organic Transistors. *Adv. Mater.* **2017**, *29*, No. 1700411.
(36) He, D.; Zhang, Y.; Wu, Q.; Xu, R.; Nan, H.; Liu, J.; Yao, J.; Wang, Z.; Yuan, S.; Li, Y. Two-Dimensional Quasi-Freestanding Molecular Crystals for High-Performance Organic Field-Effect Transistors. *Nat. Commun.* **2014**, *5*, No. 5162.
(37) Wang, Q.; Qian, J.; Li, Y.; Zhang, Y.; He, D.; Jiang, S.; Wang, Y.; Wang, X.; Pan, L.; Wang, J.; et al. 2D Single-Crystalline Molecular Semiconductors with Precise Layer Definition Achieved by Floating-Coffee-Ring-Driven Assembly. *Adv. Funct. Mater.* **2016**, *26*, 3191−3198.
(38) Rolin, C.; Kang, E.; Lee, J.-H.; Borghs, G.; Heremans, P.; Genoe, J. Charge Carrier Mobility in Thin Films of Organic Semiconductors by the Gated van der Pauw Method. *Nat. Commun.* **2017**, *8*, No. 14975.
(39) Bittle, E. G.; Basham, J. I.; Jackson, T. N.; Jurchescu, O. D.; Gundlach, D. J. Mobility Overestimation due to Gated Contacts in Organic Field-Effect Transistors. *Nat. Commun.* **2016**, *7*, No. 10908.
(40) Choi, H. H.; Cho, K.; Frisbie, C. D.; Sirringhaus, H.; Podzorov, V. Critical Assessment of Charge Mobility Extraction in FETs. *Nat. Mater.* **2017**, *17*, 2−7.
(41) Soeda, J.; Hirose, Y.; Yamagishi, M.; Nakao, A.; Uemura, T.; Nakayama, K.; Uno, M.; Nakazawa, Y.; Takimiya, K.; Takeya, J. Solution-Crystallized Organic Field-Effect Transistors with Charge-Acceptor Layers: High-Mobility and Low-Threshold-Voltage Operation in Air. *Adv. Mater.* **2011**, *23*, 3309−3314.
(42) Niazi, M. R.; Li, R.; Li, E. Q.; Kirmani, A. R.; Abdelsamie, M.; Wang, Q.; Pan, W.; Payne, M. M.; Anthony, J. E.; Smilgies, D.-M.; et al. Solution-Printed Organic Semiconductor Blends Exhibiting Transport Properties on Par with Single Crystals. *Nat. Commun.* **2015**, *6*, No. 8598.
(43) Blöchl, P. E. Projector Augmented-Wave Method. *Phys. Rev. B* **1994**, *50*, No. 17953.
(44) Kresse, G.; Furthmüller, J. Efficient Iterative Schemes for ab Initio Total-Energy Calculations Using a Plane-Wave Basis Set. *Phys. Rev. B* **1996**, *54*, No. 11169.
(45) Perdew, J. P.; Burke, K.; Ernzerhof, M. Generalized Gradient Approximation Made Simple. *Phys. Rev. Lett.* **1996**, *77*, 3865.
(46) Grimme, S. Semiempirical GGA-Type Density Functional Constructed with A Long-Range Dispersion Correction. *J. Comput. Chem.* **2006**, *27*, 1787−1799.

DOI: 10.1021/acsami.8b09655
ACS Appl. Mater. Interfaces 2018, 10, 35395−35403